PAPER

Porosity meets robustness: design of ultralight MXene/PVA composite foams for high-performance flexible supercapacitors

Zifang Zhao, [ID] [a] Zhilong Xu,[a] Weifeng Huang,[a] Jingteng Feng,[a] Guangri Xu,[ID] [a] Yuanchao Li,[ID] [a] Yalei Wang,*[b] Qichong Zhang*[c] and Wai-Yeung Wong [ID] *[d]

The conventional electrodes of flexible supercapacitors often suffer from poor mechanical properties or low specific capacitance, which significantly impedes their application in flexible electronics. Herein, MXene/PVA composite foams with porous structures were controllably fabricated. Compared with many reported MXene/polymer electrodes that enhance mechanical robustness, such MXene/PVA foams are designed to simultaneously achieve high strength and superior electrochemical performance for flexible supercapacitors. On one hand, the hydrogen bonding formed between MXene sheets and PVA molecules effectively improves the mechanical performance of the composite foams. On the other hand, the construction of continuous ion transport channels in MXene/PVA foams efficiently restrains restacking of MXene sheets and promotes rapid ion transport during electrochemical reactions, thus improving the electrochemical performance. Therefore, flexible supercapacitors based on MXene/PVA foams deliver a high specific gravimetric capacitance of 240.77 F g^{-1} and areal capacitance of 66.21 mF cm^{-2}, superior rate capability, and long-term cycle stability (12 000 cycles at 2.0 A g^{-1} with 100% capacitance retention). More importantly, the device exhibits robust electrochemical stability under diverse mechanical deformations, including bending at multiple states and 1200 cycle bending endurance testing, with negligible degradation in capacitance and Coulombic efficiency.

1. Introduction

Rapid development in electronic technology significantly accelerated the development and production of flexible and portable electronic devices. To meet the growing demands of flexible electronic devices, the energy supply systems should not only deliver superior electrochemical performance but also possess the characteristics of being "lightweight, thin, and flexible".[1,2] Among various energy storage devices, supercapacitors have emerged as one of the most promising candidates due to their high power density and long cycle life.[3–5] However, traditional supercapacitors are often rigid due to their electrode structures and preparation processes. When exposed to repeated mechanical deformation, the electrode structure is

frequently damaged, leading to a decline in electrochemical performance.[6] This mismatch between mechanical strength and electrochemical performance within traditional electrodes severely restricts their application in portable electronic devices. Therefore, the development of flexible supercapacitors with excellent energy storage properties and high mechanical strength is imperative.

Preparing flexible electrodes with enhanced mechanical strength and high conductivity is a critical solution to solve this problem. Freestanding electrodes without the use of inactive substrates, conductive agents and polymeric binders, not only increase the overall energy density, but also avoid the risk of active material detachment.[7,8] Furthermore, these electrodes are often light weight and compact, aligning well with the "lightweight, thin, and flexible" trend in flexible device development. Therefore, the fabrication of freestanding electrodes has become the preferred method for fabricating flexible electrodes of supercapacitors.

Among various fundamental materials employed for constructing freestanding flexible electrodes (such as MXenes, carbon nanotubes (CNTs), graphene, polymer films, *etc.*), MXenes have attracted wide interest due to their large specific surface area, rich chemical composition, and excellent electrical conductivity.[9–11] A variety of cations (H$^+$, Li$^+$, Na$^+$, K$^+$, NH$_4^+$, Mg^{2+}, Al^{3+}, *etc.*) can be electrochemically intercalated into their

[a]Xinxiang Key Laboratory of Power Battery Key Technology and Resource Recycling, School of Chemistry and Chemical Engineering, Henan Institute of Science and Technology, Xinxiang 453003, China

[b]Department of Mechanics and Aerospace Engineering, Southern University of Science and Technology (SUSTech), Shenzhen 518055, China. E-mail: yaleiwong@gmail.com

[c]Key Laboratory of Multifunctional Nanomaterials and Smart Systems, Suzhou Institute of Nano-Tech and Nano-Bionics, Chinese Academy of Sciences, Suzhou 215123, China. E-mail: qczhang2016@sinano.ac.cn

[d]Department of Applied Biology and Chemical Technology and Research Institute for Smart Energy, The Hong Kong Polytechnic University, Hung Hom, Hong Kong, China. E-mail: wai-yeung.wong@polyu.edu.hk

interlayers.[12–14] As a result, MXenes demonstrate high intercalation pseudocapacitance in supercapacitors.[15,16] Additionally, the distinctive physical and chemical properties of MXenes allow them to achieve a significantly higher volumetric energy density than carbon materials. Furthermore, MXenes can serve as fundamental building blocks for constructing flexible structures, such as MXene films or foams, either individually or in conjunction with other functional materials.[17,18] Nevertheless, the currently available MXene-based freestanding flexible electrodes still face significant challenges, including inadequate mechanical strength and degradation or failure of electrochemical performance under repeated bending deformation.[19,20] Enhancing the interlayer interaction force between MXene sheets and constructing robust MXene-based flexible electrodes are recognized as effective strategies to address these issues. In order to improve the mechanical properties of MXenes, many high strength MXene/polymer electrodes have been developed, including $Ti_3C_2T_x$–OH/CMC-PEDOT:PSS, MXene/PZS, $Ti_3C_2T_x$/APP-A, *etc.*[21–23] However, these electrodes usually exhibit a compact, densely packed layered architecture. This closely stacked structure inevitably impedes the rapid infiltration and transport of electrolyte ions, posing a significant limitation for applications requiring high ionic conductivity and fast electrochemical kinetics.

Poly(vinyl alcohol) (PVA), a widely used gel electrolyte matrix material, possesses abundant hydroxyl groups and other oxygen-containing functional groups, capable of forming strong intermolecular hydrogen bonds.[24,25] Although intrinsically insulating and electrochemically inert, PVA is deliberately incorporated not to mediate electronic conduction, but to concurrently reinforce structural integrity, optimize electrode–electrolyte interfaces, and facilitate ion transport. Specifically, PVA infiltrates the interlayer galleries of MXenes, where it forms stable hydrogen bonds with surface terminations, thereby enhancing mechanical flexibility and tensile strength. Concurrently, the presence of PVA can also effectively fill defects that arise during the MXene assembly process, thereby ensuring the long-term stability and reliability of flexible electrodes. Its intrinsic self-adhesive nature further promotes intimate, low-resistance contact between the active material and current collector, minimizing interfacial charge transfer resistance. Therefore, the construction of MXene/PVA composite electrodes shows great significance for the fabrication of high strength flexible electrodes.

Constructing a three-dimensional (3D) porous architecture represents an effective strategy to prevent the formation of densely packed structures commonly observed in other MXene/polymer composite systems with high strength. In addition, like other two-dimensional materials, monolayer or few-layer MXene sheets are prone to aggregation due to interlayer forces, which markedly reduces their specific surface area, impedes the effective utilization of surface active sites, and decelerates diffusion kinetics during cycling.[26,27] These factors severely compromise the electrochemical performance of MXene films. Constructing 3D porous structures can inhibit the aggregation of MXene layers and enable full exposure of active sites to electrolyte ions, thereby improving the utilization

efficiency of active materials during charge–discharge processes and substantially enhancing the electrochemical performance of electrode materials.[28–32] However, such a porous structure is prone to collapse during electrolyte wetting and charge–discharge cycles. The incorporation of PVA may avoid this phenomenon. The hydrogen bonds formed between PVA chains and MXene sheets can create a resilient, interpenetrating network that mechanically stabilizes the entire 3D porous architecture during repeated deformation, ensuring long-term cycle stability.

Based on the above considerations, we propose and experimentally validate a central hypothesis in this work: the synergistic integration of a 3D porous architecture with a robust hydrogen-bonded network between MXene sheets and PVA chains can overcome the longstanding performance trade-off between mechanical flexibility and electrochemical efficiency in flexible electrode design. Hierarchical porosity enables fast ion diffusion and maximizes electroactive surface area while hydrogen bonding improves mechanical cohesion and suppresses pore collapse during deformation. To test this hypothesis, we fabricate freestanding and flexible MXene/PVA foams *via* a hydrazine-induced foaming treatment of MXene/PVA composite films in this work. Although numerous MXene-based porous and flexible electrodes have been developed, their structural porosity often compromises mechanical robustness. The rational design of electrodes that simultaneously achieve high porosity and superior mechanical robustness remains a significant challenge. Our MXene/PVA composite foams exhibit a well-defined 3D cross-linked porous structure and excellent mechanical performance. Therefore, the flexible supercapacitors based on the composite foams demonstrate superior electrochemical performance even under different bending states and 1000 cycle bending endurance, confirming our hypothesis.

2. Results and discussion

Fig. 1a schematically presents the fabrication process of high strength MXene/PVA composite foams. In this study, $Ti_3C_2T_x$ (where T denotes functional groups such as –F, –O, and –OH) with high conductivity, large specific surface area, and superior mechanical properties was selected as active materials for flexible supercapacitors. The LiF and HCl selective etching method was used to synthesize the $Ti_3C_2T_x$ MXene suspension. The raw material of Ti_3AlC_2 consists of bulk particles with size ranging from several to tens of micrometers (Fig. S1). After selective etching and sonication, a homogeneously dispersed $Ti_3C_2T_x$ suspension was achieved (Fig. 2a). X-ray diffraction (XRD) patterns reflect the structural evolution in this procedure (Fig. 2b). The XRD spectrum of Ti_3AlC_2 shows characteristic peaks corresponding to the standard spectrum (JCPDS 52-0875). After selective etching and sonication, the prominent peaks corresponding to the (103), (104), (105) and (107) planes disappeared. A distinct peak shift of the (002) peak from 9.5° to 6.5° was observed, indicating the increase in interlayer space. These findings confirm the successful removal of the Al layer from Ti_3AlC_2. In order to analyze the morphology of MXenes,

scanning electron microscopy (SEM) and transmission electron microscopy (TEM) characterization were performed. SEM images of MXene sheets on a silicon wafer show the lamellar structure of MXenes, with the layer size less than 1 μm (Fig. S2). The freeze-dried $Ti_3C_2T_x$ reveals a porous structure composed of $Ti_3C_2T_x$ sheets (Fig. S3). The TEM image in Fig. 2c displays an ultrathin MXene flake that is nearly transparent to the electron beam. The selected area electron diffraction (SAED, inset of Fig. 2c) pattern reveals a typical sixfold symmetric diffraction pattern, suggesting the high crystallinity of $Ti_3C_2T_x$.

In a typical procedure, a predetermined amount of PVA solution was first incorporated into the $Ti_3C_2T_x$ suspension. The mixture was subsequently dispersed through ultrasonication and stirring at room temperature. The PVA content was
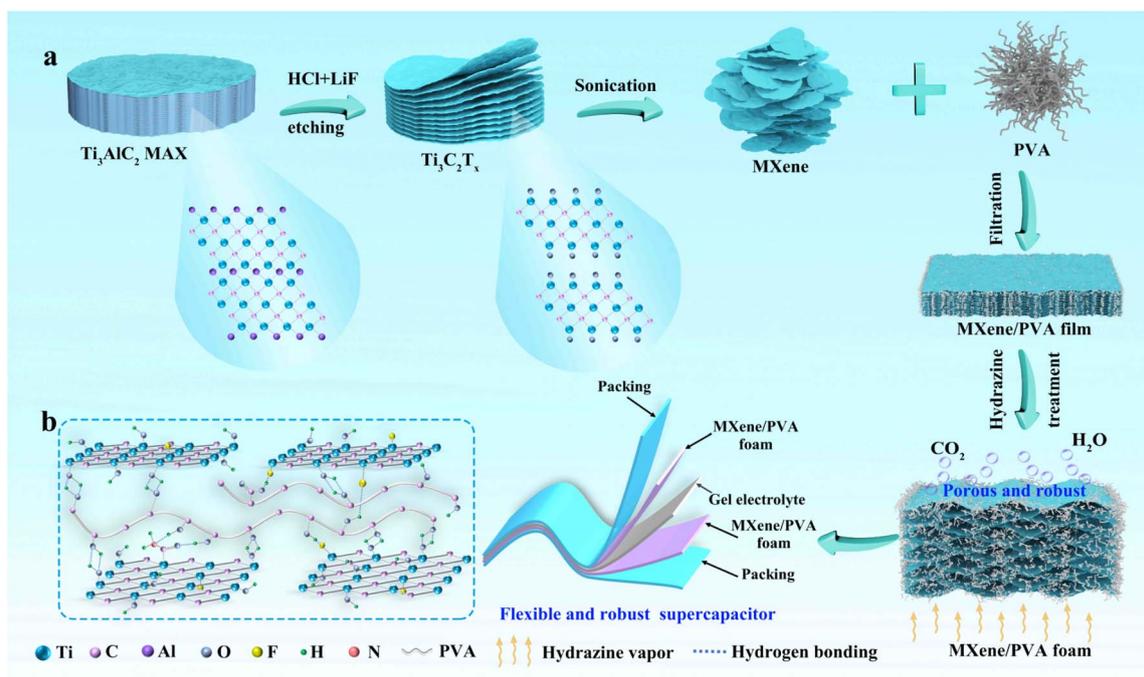

Fig. 1 (a) Schematic illustration of the fabrication process for flexible and mechanically robust supercapacitors based on MXene/PVA composite foams. (b) Schematic diagram describing the hydrogen bonding interaction between MXene sheets and PVA chains.
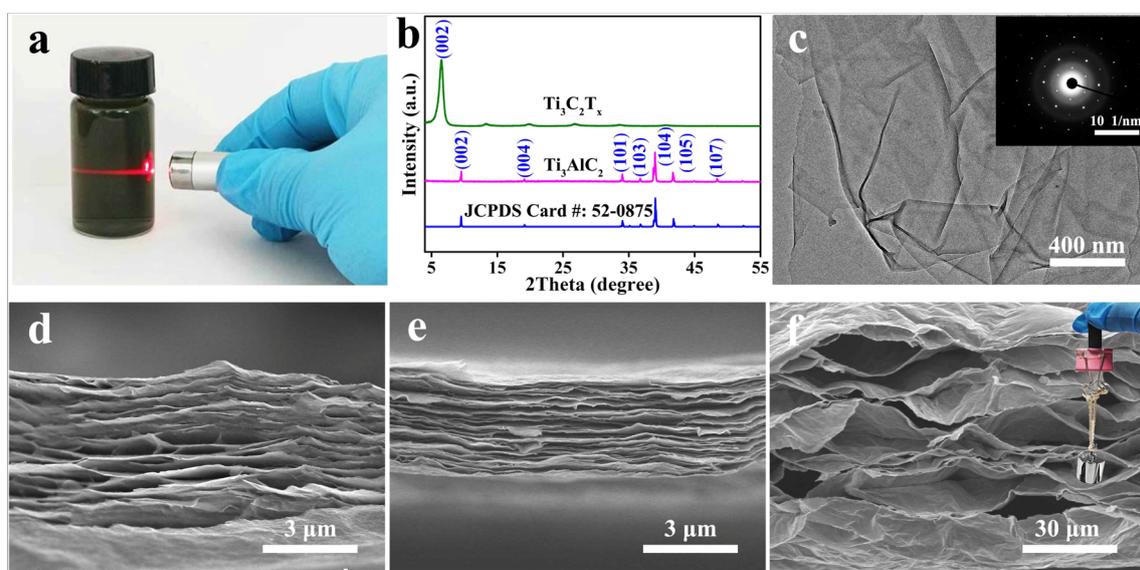

Fig. 2 (a) An optical image showing the Tyndall scattering effect in a $Ti_3C_2T_x$ suspension. (b) XRD patterns of Ti_3AlC_2 and $Ti_3C_2T_x$. (c) TEM image of an MXene sheet (inset shows the SAED pattern of $Ti_3C_2T_x$ MXene). SEM images of (d) an MXene film, (e) an MXene/PVA film, and (f) an MXene/ PVA foam (inset shows the optical image of a piece of MXene/PVA composite foam which supports a weight of 50 g), respectively.

controlled by adjusting the amount introduced. In the $Ti_3C_2T_x$/PVA mixture, PVA molecules can readily adhere to $Ti_3C_2T_x$ sheets as a result of the hydrogen bonding interactions between functional groups on the surface of $Ti_3C_2T_x$ and hydroxyl groups on PVA chains. This interaction facilitates stable couplings between $Ti_3C_2T_x$ and PVA, as illustrated in Fig. 1b. A vacuum-assisted filtration method was employed to prepare $Ti_3C_2T_x$ films and $Ti_3C_2T_x$/PVA films (denoted as MPx, where x represents the mass ratio of PVA in the composite films, x = 1, 5, 10, 15, and 20 wt%, respectively). The resulting freestanding films (Fig. S4) exhibit excellent mechanical strength and high flexibility that allow repeated folding and stretching. However, the compact layered structure of MPx films usually leads to limited ion accessible surface area, resulting in undesired electrochemical performance. In contrast, MXene foams with abundant pores benefit fast electrolyte ion diffusion and can lead to more sufficient utilization of active sites, thus improving the device performance. As a result, we prepare lightweight $Ti_3C_2T_x$/PVA foams (Fig. S4) by treating $Ti_3C_2T_x$/PVA films with hydrazine at 90 °C. Hydrazine functions as both a porogenic agent and chemical reductant. During processing, it decomposes to release gases, enabling the fabrication of lightweight and porous architectures. Concurrently, it chemically reduces MXenes by removing a portion of oxygen-containing functional groups. This reduction induces a critical shift in surface chemistry from hydrophilic to hydrophobic, which substantially improves the environmental stability and long-term durability under humid conditions.

The hydrophilic nature of MXene sheets combined with the numerous small channels formed during vacuum filtration (Fig. 2d) facilitates the penetration of hydrazine molecules into the MXene films, promoting the development of a cellular structure. As a result, after treating MXene films with hydrazine,

a 3D continuous structure formed and significant volume expansion was observed (Fig. S5), confirming the successful fabrication of the lightweight MXene foams (denoted as MHx, where x represents the hydrazine employed, x = 1, 5, 10, and 20 μL cm^{-2}, respectively). In addition, the porous structure exhibits little change when the amount of hydrazine used exceeds 5 μL cm^{-2}. Therefore, 5 μL cm^{-2} hydrazine was employed for preparing MXene/PVA composite foams (denoted as MPHx, where x represents the mass ratio of PVA in the composite foams, x = 1, 5, 10, 15, and 20 wt%, respectively). After integration with PVA, the MPx films still retain their well-organized layered configuration, except for the gradually shrinking channels as the content of PVA increases (Fig. 2e and S6), which can be ascribed to the formation of hydrogen bonds or other types of chemical bonding between MXene sheets and PVA chains.[33] This improves the mechanical performance of the composite films, benefiting the construction of high strength MXene/PVA foams. Upon foaming, numerous macropores with a pore size larger than 2 μm were generated between the parallel layers, leading to the formation of well-defined porous MXene/PVA foams (Fig. 2f, S7, and S8). Although the porous structure is not conducive to the improvement of mechanical properties, the MXene/PVA foams still deliver excellent mechanical strength and can support a weight of 50 g (inset of Fig. 2f) as a result of the strong interaction between MXene sheets and PVA molecules.

In the X-ray diffraction (XRD) patterns (Fig. 3a) of MHx treated with different amounts of hydrazine, the characteristic (002) peak demonstrates little shift, indicating that the foaming process does not affect the layer space. For MPx, the XRD patterns show only the MXene diffraction peak, and the PVA peaks at approximately 19.1° disappeared, suggesting that PVA molecules were homogeneously dispersed into MXene sheets
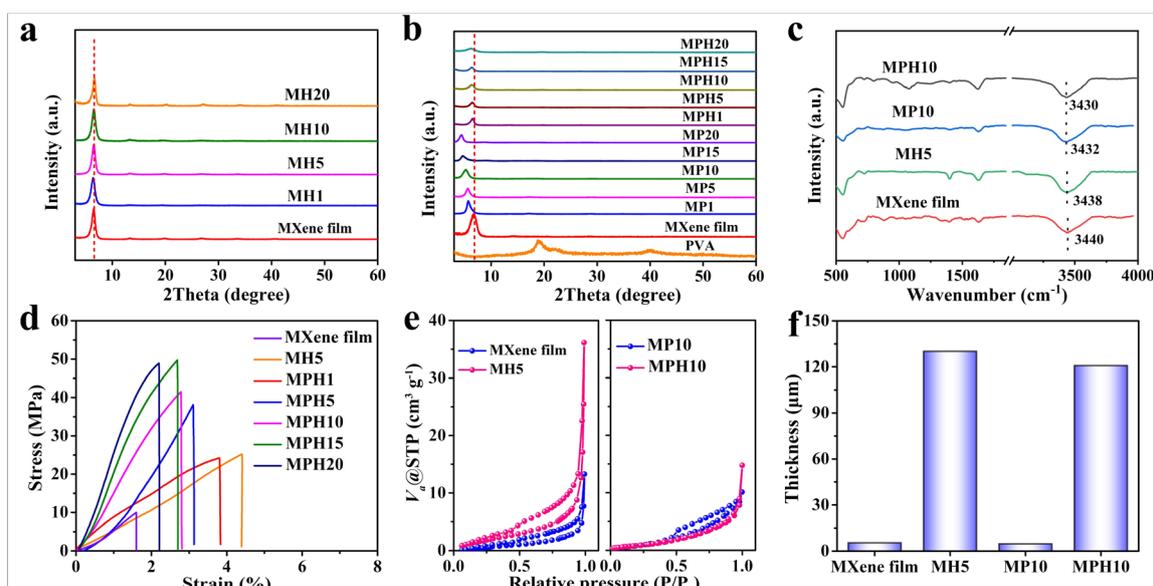

Fig. 3 XRD plots of (a) MXene films and MH1–20 as well as (b) PVA, MXene films, MP1–20, and MPH1–20, respectively. (c) FTIR spectra, (e) N₂ adsorption/desorption curves, (d) stress–strain curves, and (f) the thickness variation of an MXene film, MH5, MP10, and MPH10, respectively.

(Fig. 3b). In addition, the layer space of the composite films increases with the increase in PVA content, as suggested by the obvious (002) peak shift to a lower angle in their XRD patterns. This indicates that PVA molecules were inserted between MXene sheets. However, after treating the composite films with hydrazine, the (002) peak shifts to a higher angle, which may be caused by the enlarged interface bonding force between MXenes and PVA chains induced by hydrazine, the decreased water amount between MXene layers after thermal treatment, or the weakened electrostatic repulsive force caused by the decrease in hydrophilic functional groups (confirmed by the XPS and water contact angle results) (Fig. 4a–f).[21,34–36] The specific changes in layer space are shown in Fig. S9. In the Fourier transform infrared (FTIR) spectra, the –OH peak of MXene films (3440 cm^{-1}) exhibits a redshift to 3432 cm^{-1} in MP10 and to 3430 cm^{-1} in MPH10, respectively, indicating the formation of hydrogen bonding between MXene sheets and PVA chains (Fig. 3c and S7). The strong interfacial coupling between MXenes and PVA chains endows the MPs and MPHs with excellent mechanical properties, which is reflected in their stress–strain curves (Fig. 3d and S10). As a result, the tensile strength and Young's modulus of MPH20 reach 48.93 MPa and 2.22 GPa (Fig. 3d and S11), respectively, which are approximately 1.94 and 3.89 times higher than those of the pure MXene foams (tensile strength: 25.21 MPa; Young's modulus: 0.57 GPa). Moreover, these mechanical properties exceed those of many reported porous MXene/polymer composites (Fig S12).[37–43] Although the mechanical performance of MP1-20 is also higher than that of MPH1-20, this aligns with the fundamental materials science principles: the introduction of porosity generally leads to the reduction of the material's mechanical strength. Besides the excellent mechanical properties, MPHs also exhibit a cellular structure. As reflected in their N$_2$ adsorption–desorption isotherms, all MXene-based samples except MPH10 exhibit type-IV isotherms with a hysteresis loop, corresponding to the slit-like holes in the samples (Fig. 3e). These characteristics suggest the coexistence of macropores and mesopores. The specific surface area of MH5 is 7.42 m^2 g^{-1}, which is significantly higher than that of pure MXene films (4.79 m^2 g^{-1}). However, the introduction of PVA enhances the interface force between MXene sheets due to the formation of hydrogen bonding, thereby making pore formation more challenging. Therefore, the remaining micropores cannot be transformed into mesopores during the foaming process, and only weak adhesion areas (mesopores or macropores) can be expanded to form macropores, which is proved by the disappearance of hysteresis loops in its N$_2$ adsorption–desorption isotherms. Although the formation of macropores is in favor of the improvement of specific surface area, the limitations of the N$_2$ adsorption–desorption measurement result in only a minor difference in the measured specific surface area between MPH10 and the pure MXene films. Nevertheless, the variation in thickness during the foaming process in Fig. 3f confirmed the formation of a porous structure. The average thickness of the MXene films and MP10 is 5.3 and 4.8 μm, respectively. After the hydrazine treatment, a noticeable change in their thickness is observed. Specifically, the average thickness of MH5 and

MPH10 increased to 129.1 and 121.8 μm, respectively, which is approximately 24.3 and 25.4 times higher than that in their unfoamed state (Fig. 3f). As a result of the strengthened pore architecture arising from the hydrogen bonding between MXene sheets and PVA chains, the expansion of MPHs during foaming is constrained. Consequently, the average thickness of MPH10 is lower than that of MH5. This dramatic thickness enhancement proved the development of a porous structure during the foaming process, which facilitates rapid ion/electron transport through interconnected channels, thus significantly boosting the electrochemical performance.

The excellent physical properties of MXene/PVA composite foams largely depend on their foaming mechanism. To further explore their foaming process, we performed XPS and contact angle measurements to analyze their chemical conversion during the foaming process. It is noted that XPS survey spectra of all MXene-based samples reveal the presence of Ti, C, O, and F elements (Fig. 4a). And there is almost no detectable Al 2p signal in all samples, indicating the complete etching of Al. After the foaming process, the peak ascribed to N 1s appears at 400.7 eV for the MH5 and MPH10 foams, which may originate from the chemical reaction between MXenes and hydrazine under thermal treatment. The presence of the nitrogen element expands the interlayer spacing of MXene sheets and creates abundant defects and active sites, significantly boosting pseudocapacitance *via* reversible surface redox reactions.[35,44,45] The high resolution spectra reveal that the C 1s and O 1s peaks exhibit little change compared with those of MXene films (Fig. 4b, d and Tables S2, S3). However, the foaming process leads to a slight increase in both the C/O ratio (from 1.54 to 1.72) and the Ti/O ratio (from 1.16 to 1.19), suggesting partial removal of oxygen-containing functional groups (Table S1). The reducing role of hydrazine is further supported by a control experiment in which water replaced hydrazine under otherwise identical conditions, resulting in severe oxidation of MXene films. As shown in Fig. S13, the C 1s and O 1s spectra of the water-treated MXene/PVA films exhibit a pronounced enhancement in peaks corresponding to oxygen-containing groups (C–O, C=O, and Ti–O/O–H). After the incorporation of PVA, the peaks of C–O, and C=O in the C 1s spectra and the peaks of Ti–O/O–H, and C–O in the O 1s spectra of the MPH10 sample obviously weakened compared with that of MP10 (Fig. 4c, e and Tables S2, S3). Correspondingly, the C/O atomic ratio increases markedly from 2.26 to 3.28, and the Ti/O atomic ratio increases from 0.92 to 1.21 (Table S1). Unlike the modest changes seen in samples without PVA, this pronounced shift indicates that PVA significantly enhances the thermal stability of MXenes,[33,46–48] which benefits the application of MXene-based devices in extreme environments. These chemical changes are consistent with variations in surface wettability. Owing to the existence of oxygen and fluorine functional groups, pure MXene films show a typical hydrophilic nature, demonstrated by the water contact angle of 48.5° (Fig. 4f). After the foaming process, the water contact angle of MH5 exhibits little difference compared with that of MXene films. Upon the incorporation of PVA, the water contact angle moves to a higher value, as a result of the weaker hydrophilic nature of PVA
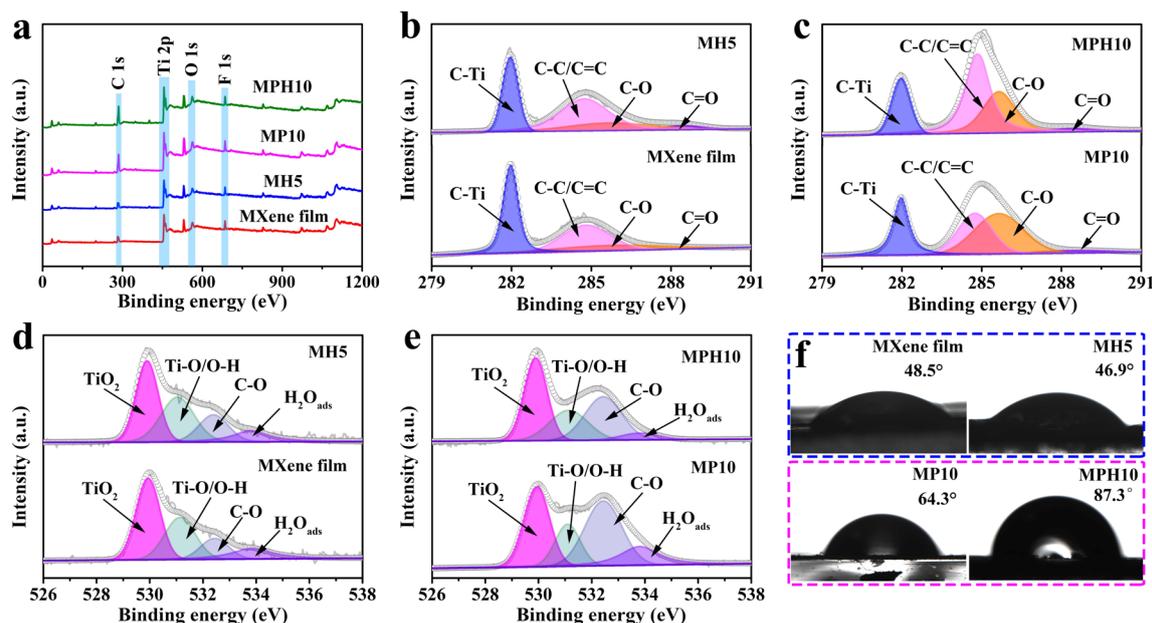
Fig. 4 (a) XPS survey spectra, (b and c) C 1s spectra, (d and e) O 1s spectra, and (f) the water contact angle of MXene films, MH5, MP10, MPH10, respectively.

compared with MXenes. However, after the foaming process, the water contact angle of MPH10 significantly increased to 87.3°, close to the hydrophobic state, once again proving the reduction of MXenes by hydrazine during the foaming process. All these results are consistent with the previously published literature.[35]

To explore the effect of different hydrazine amounts used during the foaming process and the PVA content on the electrochemical properties of the MXene-based electrodes, a two electrode system with 1 M H_2SO_4 as electrolyte was employed. Fig. S14a and b shows the cyclic voltammetry (CV) and galvanostatic charge/discharge (GCD) plots of MH1-20 compared with MXene films. The CV curves of MXene films and MH1-20 (Fig. S15) exhibit near-rectangular shapes, which indicate the low resistance and good reversibility of the charging/discharging process. The enclosed area of the MXene films and MH1-20 increased with the increase in hydrazine when the amount of hydrazine is less than 5 μL cm^{-2} and then decreased when more hydrazine is employed, indicating the highest specific capacitance of MH5. Moreover, the GCD plots of MXene films and MH1-20 (Fig. S16) exhibit almost symmetrical triangular shapes, and MH5 shows the longest discharge time, well consistent with the CV results. In order to get an overview of the effects of different hydrazine amounts, specific capacitance of MXene films and MH1-20 is calculated (Fig. S14c). As expected, the specific capacitance decreased with the scan rate as a result of the limited migration of electrolyte into the interior part of electrodes. In addition, MH5 displays the highest specific capacitance among all scan rates. These results can be attributed to the formation of more pores for ion transport in MXene foams with higher hydrazine content. However, a further increase in hydrazine dosage does not

significantly enhance pore development. In contrast, excessive hydrazine may lead to over-reduction of MXenes, reducing oxygen-containing functional groups and consequently degrading electrochemical performance. Based on this, we construct MXene/PVA foams with different PVA contents by employing 5 μL cm^{-2} hydrazine. Although moderate introduction of PVA benefits the mechanical and electrochemical properties of the composite foams, excessive PVA impedes ion transport, and thus deteriorates the electrochemical performance. The construction of a 3D porous structure sheds light on this problem. As shown in Fig. S14d–f, S17, and S18, the specific capacitance of MP1, MP5, and MP10 is enhanced a little compared with that of MXene films, especially at low scan rates or low current densities, which may be attributed to the enlarged layer space that suppresses the agglomeration of MXene films as a result of the introduction of PVA molecules. However, overuse of PVA that is inactive and nonconductive would increase the impedance of the composite films and decrease the content of the active material. As a result, MP15 and MP20 exhibit low specific capacitance. Upon foaming, besides the intercalation effect of PVA, macropores can also form between MXene sheets and primarily serve as ion transport pathways. Thus, more active sites become accessible and the electrochemical performance of MPH significantly improved. The specific capacitance of MPH10 is calculated to be 237.40 F g^{-1} (261.14 mF cm^{-2}; 43.44 F cm^{-3}) at 5 mV s^{-1}. As the scan rate increases to 100 mV s^{-1}, the specific capacitance of MPH10 is still maintained at 177.33 F g^{-1}, which is higher even when compared with the porous sample of MH5 without the incorporation of PVA (Fig. 5a–f, S19 and S20).

The MXene/PVA foams show unique structures with superior conductivity and a high porosity ratio. Consequently, they are
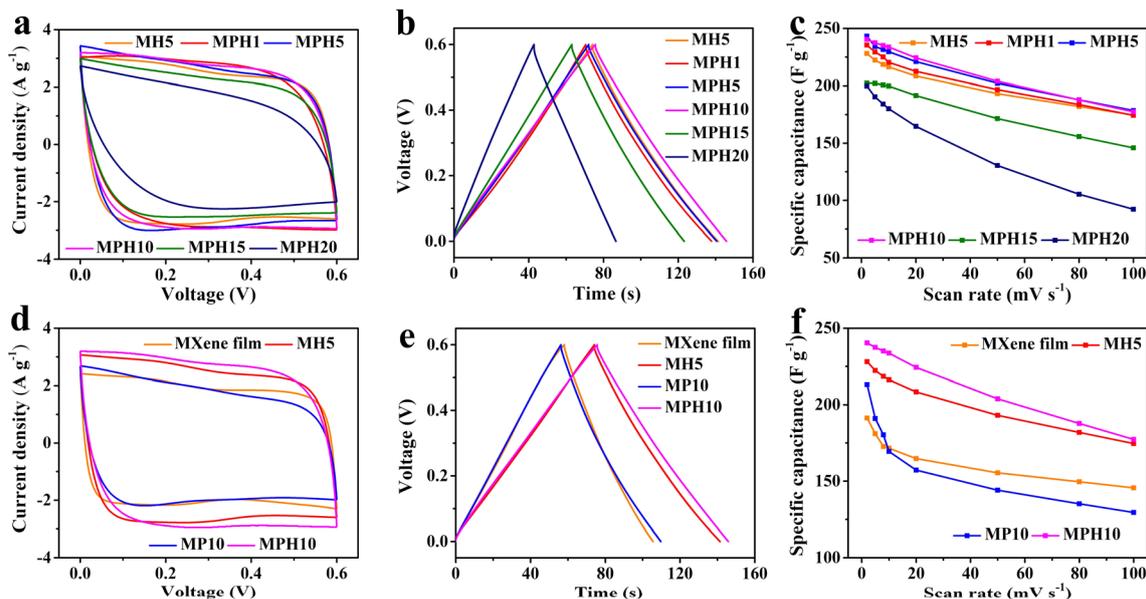
Fig. 5 Electrochemical properties of MPH1-20 *versus* MH5: (a) CV curves at 50 mV s^{-1}; (b) GCD plots at 0.5 A g^{-1}; (c) specific capacitance at different scan rates. (d) CV curves at 50 mV s^{-1}, (e) GCD plots at 0.5 A g^{-1}, and (f) specific capacitance at various scan rates of MXene films, MH5, MP10, and MPH10.

expected to be competitive electrode candidates for flexible supercapacitors. Based on MPH10, a flexible supercapacitor device was fabricated with PVA/H$_2$SO$_4$ electrolyte (Fig. 6a). As shown in Fig. 6b and S21, owing to the different ion diffusion rates in the liquid and gel electrolyte, the CV and GCD shape of the flexible supercapacitors differs slightly from that of conventional supercapacitors. The CV curves of the flexible supercapacitors display typical rectangle-like shapes (Fig. 6b),

indicating the superior capacitive behavior of MXene foams. This is further supported by their GCD curves with an isosceles triangle shape (Fig. S21 and S22). Besides, current responses of the flexible supercapacitors show a nearly linear connection with scan rates (Fig. 6d). The specific capacitance of the flexible supercapacitors is calculated to be 240.77 F g^{-1} (264.84 mF cm^{-2}; 44.06 F cm^{-3} for a single electrode) at 2 mV s^{-1}, and they can still deliver a high specific capacitance of 158.74 F g^{-1} even
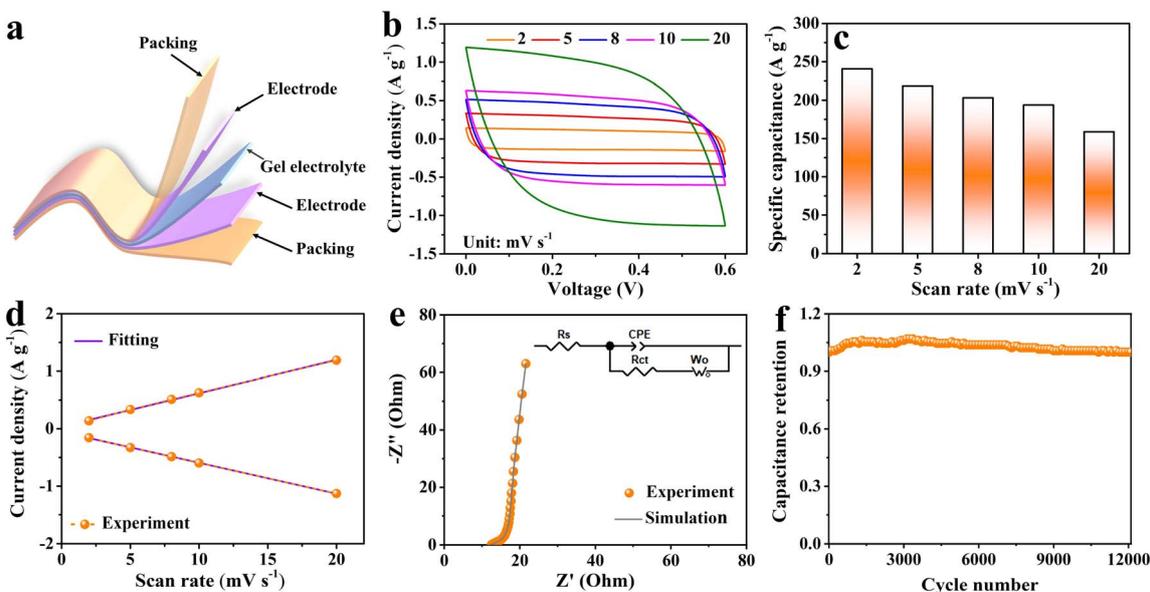

Fig. 6 (a) Schematic illustration of flexible supercapacitors. Electrochemical performance of flexible supercapacitors: (b) CV curves at various scan rates; (c) specific capacitances based on CV curves; (d) current responses from CV measurements of flexible supercapacitors; (e) Nyquist plots (100 mHz–100 kHz); (f) long-term cycle performance at 2.0 A g^{-1}.

at a high scan rate of 20 mV s^{-1} (Fig. 6c). Such superior rate performance is attributed to the fast electrochemical reaction kinetics, which can be revealed by the Nyquist plot (Fig. 6e). The data were fitted by an equivalent circuit and the results show small internal resistance (R_s, 12.51 Ω) and charge transfer impedance (R_{ct}, 0.28 Ω), indicating the fast charge-transfer capability of MPH10 due to its porous structure and high conductivity. Long-term cycle stability plays another important role in evaluating the practicality of flexible supercapacitors. Flexible supercapacitors exhibit a capacitance retention of 100% over 12 000 cycles at 2.0 A g^{-1}, demonstrating their excellent long-term cycle stability. Such performance is superior compared with many other flexible supercapacitors based on MXene/polymer electrodes (Table 1).[20,49–60]

The excellent electrochemical performance of the flexible supercapacitor based on MPH10 is intrinsically linked to its rapid ion transport kinetics, as evidenced by the well-retained rectangular shape of CV curves across a wide range of scan rates (Fig. 6b). The current (i) of the CV curves generally can be expressed as the sum of the surface capacitance-controlled current (i_{cap}) and the diffusion-controlled current (i_{diff}) with the following empirical formula:[61]

$$i = i_{cap} + i_{diff} = av^b \tag{1}$$

This equation can also be rewritten as:

$$\log(i) = b\log(v) + \log(a) \tag{2}$$

Here, v represents the scan rate while a and b are adjustable parameters. When b equals 0.5, the diffusion-controlled process dominates the electrochemical reaction. When b equals 1.0, the surface capacitance-controlled process dominates the entire electrochemical reaction. Based on formula (2), the curves of log v *versus* log i were linearly fitted (Fig. 7a). The slopes of these fitted lines are denoted by the parameter b, which varies from 0.924 to 0.949 at different potentials (Fig. 7b). This result indicates that the surface capacitance-controlled process dominates the electrochemical reaction of the flexible supercapacitors.

Besides, the capacitance contribution percent was further quantified using Dunn's method.[62] According to this method, the total current (i) at one given potential can be expressed as the sum of two components: k_1v (surface capacitance-controlled contribution) and $k_2v^{1/2}$ (diffusion-controlled contribution), where v denotes the scan rate.[63] The surface capacitance contributions at different scan rates can be visualized as areas in the CV plots (Fig. 7c and S23). It is noted that the capacitance contribution gradually increases with the scan rate. This phenomenon suggests that higher scan rates benefit the enhanced capacitance contribution, for the reason that the ion insertion and deintercalation process under such conditions are primarily confined to surface charge and discharge reactions. Moreover, the capacitance contributions at 2, 5, 8, 10 and 20 mV s^{-1} were 57.36%, 62.17%, 66.00%, 68.46% and 78.80%, respectively (Fig. 7d). These results can be attributed to the 3D cross-linked porous structure of the MPH10 electrodes that inhibits the restacking of MXene sheets and facilitates rapid ion and electron transport throughout the network. As a result, the flexible supercapacitors possess fast charge transfer kinetics.

For the purpose of evaluating potential electrochemical degradation of the flexible supercapacitors over mechanical strength, CV and GCD curves at varied bending states were obtained on the stretching platform (Fig. 8a). The initial distance between the two ends of the devices is 4.0 cm, and then they are bent into 2.7, 1.5, and 0 cm, respectively. The CV curves exhibit little distinction at different bending states (Fig. 8b). Their corresponding normalized capacitances with a length of 4.0, 2.7, 1.5, and 0.0 cm are calculated to be 225.62, 208.20, 201.69 and 200.35 F g^{-1}, respectively (Fig. 8d), suggesting the high electrochemical stability of the flexible supercapacitors. The electrochemical stability of the supercapacitors under various bending conditions can also be inferred from their almost overlapping GCD curves (Fig. 8c). Moreover, in order to evaluate the mechanical fatigue resistance of the flexible supercapacitors, GCD measurements were performed under cyclic bending (30 cycles per test). The results show negligible change in capacitance retention during 1200 bending times (the distance between the two ends of the device was bent from 4.0

Table 1 Comparisons of electrochemical performance of some MXene-based electrode materials

| Electrode materials	Electrolyte medium	Current density/scan rate	Specific gravimetric capacitance (F g^{-1})	Specific areal capacitance (mF cm^{-2})	Retention (%)	Number of cycles	Ref.
Ti$_3$C$_2$T$_x$/PVA	1 M KOH	2 mV s^{-1}			84	10 000	20
Ti$_3$C$_2$T$_x$/CNF		2 mV s^{-1}	120		98	10 000	49
Ti$_3$C$_2$T$_x$/CNC/PP	1 M H$_2$SO$_4$	10 mV s^{-1}		232	78	10 000	50
Ti$_3$C$_2$T$_x$-BOPP		0.1 mA cm^{-2}	238.8	358.2	78	2000	51
Ti$_3$C$_2$T$_x$/PDT	0.5 M H$_2$SO$_4$	50 mA cm^{-2}		284	100	10 000	52
Ti$_3$C$_2$T$_x$/SCNF	1 M H$_2$SO$_4$		220		100	5000	53
Ti$_3$C$_2$T$_x$-S-ENR	1 M H$_3$PO$_4$	0.2 A g^{-1}	283.44		86	2000	54
Ti$_3$C$_2$T$_x$/MPFs	0.5 M H$_2$SO$_4$	1 mA cm^{-3}			95.9	7000	55
Ti$_3$C$_2$T$_x$/PVA	1 M H$_2$SO$_4$	5 mV s^{-1}	119.3	130.9			56
Ti$_3$C$_2$T$_x$-AFAO	1 M H$_2$SO$_4$	1 A g^{-1}	211.2		92.0	5000	57
Ti$_3$C$_2$T$_x$/SCNF	1 M H$_2$SO$_4$	1 A g^{-1}	218.3	241.2	95.1	5000	58
Ti$_3$C$_2$T$_x$/pg-C$_3$N$_4$	1 M MgSO$_4$	2 mV s^{-1}	140			10 000	59
Ti$_3$C$_2$T$_x$	1 M Li$_2$SO$_4$	0.5 mV s^{-1}	149.8		100	10 000	60
Ti$_3$C$_2$T$_x$/PVA	2 M H$_2$SO$_4$	5 mV s^{-1}	240.77	261.14	100	12 000	This work
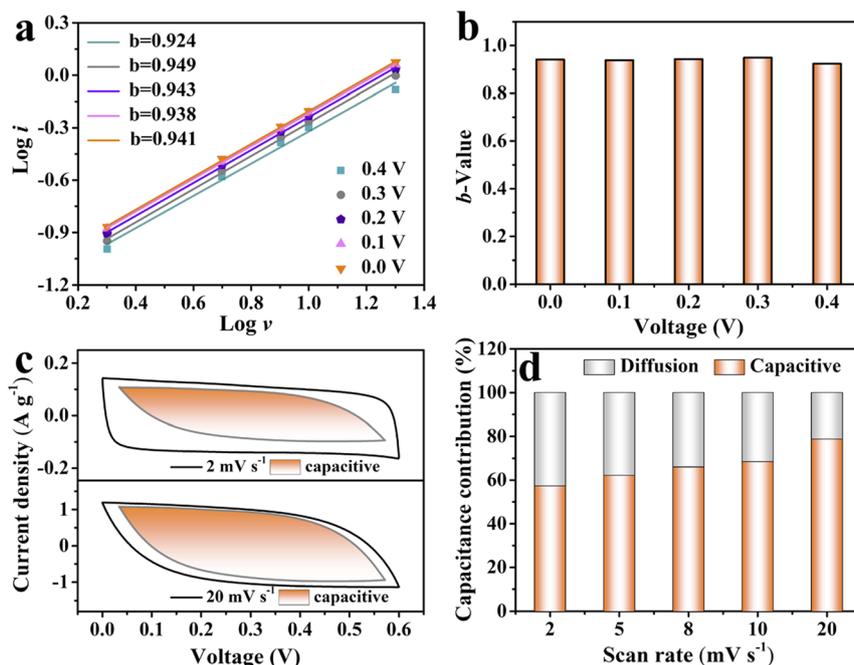
Fig. 7 Electrochemical reaction kinetic analysis of the flexible supercapacitors: (a) fitted plots of log i vs. log v at different potentials; (b) the varied b-values at different potentials; (c) CV curves with capacitance contribution at 2 and 20 mV s^{-1}; (d) capacitance contribution at various scan rates.

to 2.0 cm; see Fig. 8e). This remarkable electrochemical stability suggests that flexible supercapacitors hold great potential for use as flexible power sources. To visually demonstrate the flexibility of the devices, three supercapacitors connected in series were tested under both flat and bent configurations to power a calculator's liquid crystal display (LCD). Notably, even
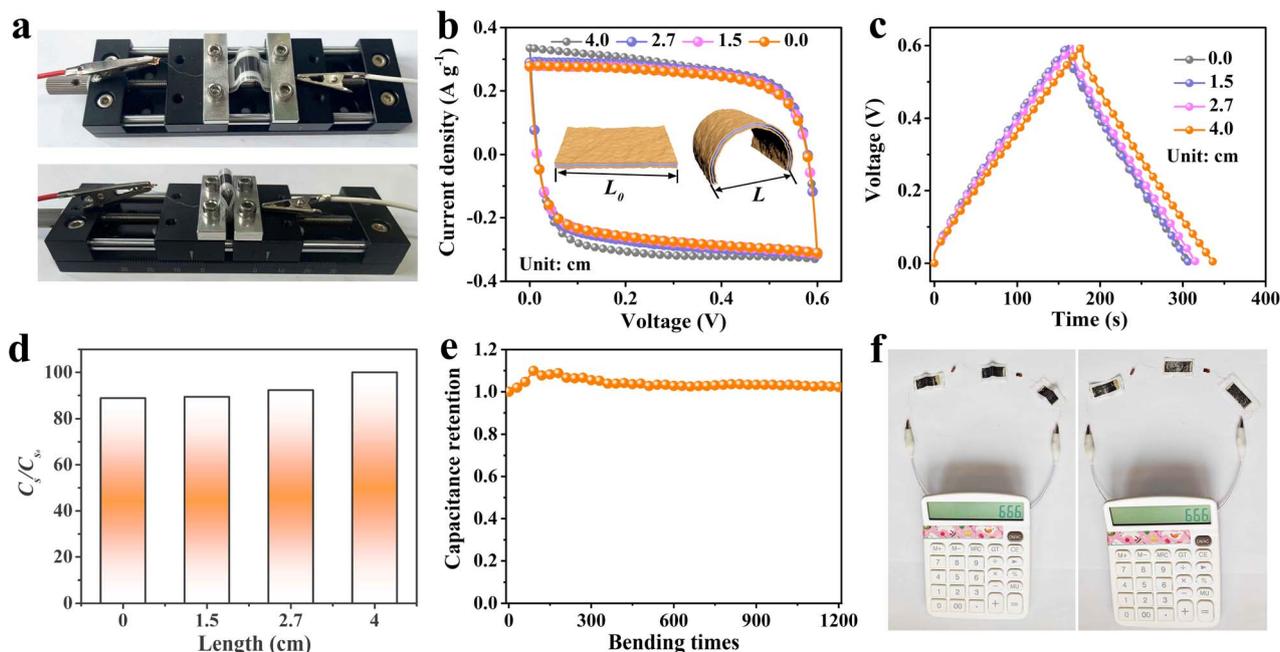
Fig. 8 (a) Optical images of the flexible supercapacitors during the bending test. (b–e) Electrochemical performance of the flexible supercapacitors (where C_{s0} and L_0 represent the initial capacitance and distance of flexible supercapacitors, and C_s and L denote the capacitance and distance under different bending states, respectively): (b) CV curves at 5 mV s^{-1}, (c) GCD plots at 0.2 A g^{-1}, and (d) normalized specific capacitances calculated from CV curves, (e) capacitance retention of the device at different bending times. (f) Optical photographs of a lit LCD under different bending states.

after being bent to a significant angle, the devices were able to stably illuminate the LCD, confirming their suitability as stretchable energy storage components (Fig. 8f).

3. Conclusions

In summary, flexible MXene/PVA composite foams were successfully prepared and applied to flexible supercapacitors. Such MXene/PVA composite foams realized the balance between mechanical strength and electrochemical performance in conventional electrodes by constructing a 3D porous structure on the high strength MXene/PVA composite films. Specifically, the introduction of PVA induces the hydrogen bonding between MXene sheets and PVA chains, which improves the mechanical properties of the composite foams. Moreover, the construction of a 3D porous structure suppresses the agglomeration of MXene sheets and promotes rapid ion transport, thus improving the electrochemical performance. Therefore, the MXene/PVA foams deliver a high tensile strength of 48.93 MPa and Young's modulus of 2.22 GPa. More importantly, the flexible supercapacitors based on the MXene/PVA foams show a high specific capacitance of 240.77 F g^{-1} and stable electrochemical performance even under various bending states and repeated bending cycles. The combination of high mechanical strength and excellent electrochemical properties of such supercapacitors makes them promising candidates for flexible and wearable electronics.

4. Experimental section

4.1 Preparation of MXenes

$Ti_3C_2T_x$ was synthesized by etching Ti_3AlC_2 using a LiF/HCl solution. Typically, 2 g of LiF (Alfa Aesar) was first dissolved in 40 mL of 6 M HCl under continuous stirring. Subsequently, 2 g of Ti_3AlC_2 was added to the resulting solution, which was then heated to 45 °C. After reacting for 72 hours at this temperature with continuous stirring, the product was collected and repeatedly washed with deionized water until the pH approached approximately 6. Thereafter, 200 mL of deionized water was added to the resulting precipitate. Following ultrasonication and centrifugation at 3500 rpm for 30 minutes, a well-dispersed $Ti_3C_2T_x$ suspension with a yield of approximately 50% was successfully obtained.

4.2 Fabrication of MXene/PVA foams

A well-dispersed MXene/poly(vinyl alcohol) (PVA) suspension was initially prepared by mixing the MXene suspension (0.3 mg mL^{-1}) with the PVA solution (1 mg mL^{-1}). The PVA content was precisely controlled by adjusting the volume of the PVA solution. Subsequently, the MXene/PVA films were obtained via vacuum filtration of the above MXene/PVA suspension using a polypropylene membrane (Celgard 2400). The thickness of the films was tailored by varying the concentration and volume of the suspension. After that, a piece of freestanding MXene/PVA film was coated with hydrazine monohydrate (80%, coating amount: 5 μL cm^{-2}) and then heated at 90 °C for 3 h to fabricate

MXene/PVA foams. For comparison, pure MXene foams were also prepared with identical steps without the presence of PVA.

4.3 Fabrication of conventional supercapacitors

Conventional supercapacitors were assembled to assess the fundamental electrochemical characteristics of the electrodes. Pt slices functioned as current collectors, while filter paper acted as the separator. The MXene-based electrodes and separator were layered together, with the 1 M H_2SO_4 electrolyte introduced between them.

4.4 Fabrication of flexible supercapacitors

The PVA/H_2SO_4 electrolyte was prepared by dissolving 1 g of PVA in a solution containing 1 g of concentrated H_2SO_4 and 10 mL of deionized water. The mixture was then heated to 85 °C under continuous stirring till it became transparent. Subsequently, two identical rectangular shaped MXene/PVA foam electrodes with a size of 3 × 1 cm^2 and areal loading of 1.1 mg cm^{-2} were placed on polyethylene terephthalate (PET) substrates. The PVA/H_2SO_4 gel electrolyte was then added dropwise and dried under vacuum conditions. Finally, a piece of filter paper was sandwiched between two identical MXene films, completing the fabrication of the flexible supercapacitors. Afterwards, it was sealed by using a piece of polyethylene terephthalate film.

4.5 Material characterization

The morphology features of the materials were analyzed by scanning electron microscopy (SEM, Hitachi SU8010) and transmission electron microscopy (TEM, FEI Talos F200X G2). X-ray diffraction (XRD, Bruker D8 Advance A25) was employed to investigate the crystal structure of materials. X-ray photoelectron spectroscopy (XPS, ESCALAB Xi+, Thermo Fisher Scientific, USA) was used to determine the elemental composition and oxidation states of the samples and the contact angles were measured using an SDC-100 system. Specific surface area of the material was measured by using an nitrogen adsorption isotherm tester (Quantachrome 4000nova). Fourier transform infrared spectra (FTIR) were obtained on a BIORAD FTS 600.

Author contributions

Zifang Zhao: conceptualization, data curation, funding acquisition, writing – original draft, writing – review & editing; Zhilong Xu: investigation, project administration, writing – original draft; Weifeng Huang: funding acquisition, conceptualization, formal analysis, writing – review & editing; Jingteng Feng: investigation, project administration; Guangri Xu: formal analysis, investigation, methodology; Yuanchao Li and Yalei Wang: supervision, project administration; Qichong Zhang: formal analysis, methodology, resources; Wai-Yeung Wong: writing – review & editing, resources, conceptualization.

Conflicts of interest

There are no conflicts to declare.

Data availability

The data supporting this article have been included as part of the supplementary information (SI). Supplementary information: SEM, XPS, pore size distribution curves, stress–strain curves, the comparison of tensile strength and Young's modulus, electrochemical performance. See DOI: https://doi.org/10.1039/d6ta00010j.

Acknowledgements

References

1 D. P. Dubal, N. R. Chodankar, D.-H. Kim and P. Gomez-Romero, *Chem. Soc. Rev.*, 2018, **47**, 2065–2129, DOI: 10.1039/C7CS00505A.

2 I. Hussain, S. Sahoo, M. S. Javed, J. Lu and K. Zhang, *Mater. Sci. Eng., R.*, 2024, **160**, 100814, DOI: 10.1016/j.mser.2024.100814.

3 Y. Shao, M. F. El-Kady, L. J. Wang, Q. Zhang, Y. Li, H. Wang, M. F. Mousavi and R. B. Kaner, *Chem. Soc. Rev.*, 2015, **44**, 3639–3665, DOI: 10.1039/C4CS00316K.

4 J. Y. Zhang, Y. Liu, X. S. Zhang, L. Y. Xue, L. L. Zhang and X. Y. Liu, *Energy Environ. Mater.*, 2026, **9**, e70098, DOI: 10.1002/eem2.70098.

5 H. Cao, Y. Zhang, X. Zhou, J. Yu, X. Chen and L. Li, *Chem. Commun.*, 2024, **60**, 14629–14632, DOI: 10.1039/d4cc04275a.

6 Z. Zhao, S. Wang, F. Wan, Z. Tie and Z. Niu, *Adv. Funct. Mater.*, 2021, **31**, 2101302, DOI: 10.1002/adfm.202101302.

7 H. Xu, J. Fan, H. Su, C. Liu, G. Chen, Y. Dall'Agnese and Y. Gao, *Nano Lett.*, 2023, **23**, 283–290, DOI: 10.1021/acs.nanolett.2c04320.

8 Z. Zhao, X. Wang, M. Yao, L. Liu, Z. Niu and J. Chen, *Chin. Chem. Lett.*, 2019, **30**, 915–918, DOI: 10.1016/j.cclet.2019.03.003.

9 J. Pang, R. G. Mendes, A. Bachmatiuk, L. Zhao, H. Q. Ta, T. Gemming, H. Liu, Z. Liu and M. H. Rummeli, *Chem. Soc. Rev.*, 2019, **48**, 72–133, DOI: 10.1039/c8cs00324f.

10 S. P. Vinodhini, J. Christina X, P. Kumaresan, G. Anitha and J. R. Xavier, *J. Power Sources*, 2026, **661**, 238651, DOI: 10.1016/j.jpowsour.2025.238651.

11 L. Xue, Y. Liu, Z. Chen, J. Zhang, Z. Luo and L. Zhang, *Small*, 2025, **21**, 2412496, DOI: 10.1002/smll.202412496.

12 O. Mashtalir, M. Naguib, V. N. Mochalin, Y. Dall'Agnese, M. Heon, M. W. Barsoum and Y. Gogotsi, *Nat. Commun.*, 2013, **4**, 1716, DOI: 10.1038/ncomms2664.

13 S. Kajiyama, L. Szabova, K. Sodeyama, H. Iinuma, R. Morita, K. Gotoh, Y. Tateyama, M. Okubo and A. Yamada, *ACS Nano*, 2016, **10**, 3334–3341, DOI: 10.1021/acsnano.5b06958.

14 M. R. Lukatskaya, O. Mashtalir, C. E. Ren, Y. Dall'Agnese, P. Rozier, P. L. Taberna, M. Naguib, P. Simon, M. W. Barsoum and Y. Gogotsi, *Science*, 2013, **341**, 1502–1505, DOI: 10.1126/science.1241488.

15 Z. Zhao, Z. Xu, Y. Wang, W. Huang, Y. Cheng and W.-Y. Wong, *J. Mater. Chem. A*, 2025, **13**, 13175–13185, DOI: 10.1039/d5ta00327j.

16 X. J. Christina, S. P. Vinodhini, G. Anitha and J. R. Xavier, *J. Mater. Sci.*, 2025, **60**, 10632–10669, DOI: 10.1007/s10853-025-11092-1.

17 H. Li, Y. Hou, F. Wang, M. R. Lohe, X. Zhuang, L. Niu and X. Feng, *Adv. Energy Mater.*, 2017, **7**, 1601847, DOI: 10.1002/aenm.201601847.

18 J. Liu, H. B. Zhang, R. Sun, Y. Liu, Z. Liu, A. Zhou and Z. Z. Yu, *Adv. Mater.*, 2017, **29**, 1702367, DOI: 10.1002/adma.201702367.

19 C. Rong, T. Su, T. Chu, M. Zhu, B. Zhang and F.-Z. Xuan, *Small*, 2025, **21**, 2411329, DOI: 10.1002/smll.202411329.

20 Z. Ling, C. E. Ren, M.-Q. Zhao, J. Yang, J. M. Giammarco, J. Qiu, M. W. Barsoum and Y. Gogotsi, *Proc. Natl. Acad. Sci. U. S. A*, 2014, **111**, 16676–16681, DOI: 10.1073/pnas.1414215111.

21 J. Cao, C. Chen, K. Chen, Q. Lu, Q. Wang, P. Zhou, D. Liu, L. Song, Z. Niu and J. Chen, *J. Mater. Chem. A*, 2017, **5**, 15008–15016, DOI: 10.1039/C7TA04920J.

22 L. Gao, C. Li, W. Huang, S. Mei, H. Lin, Q. Ou, Y. Zhang, J. Guo, F. Zhang, S. Xu and H. Zhang, *Chem. Mater.*, 2020, **32**, 1703–1747, DOI: 10.1021/acs.chemmater.9b04408.

23 Z. Lu, Y. Wu, L. Ding, Y. Wei and H. Wang, *Angew. Chem., Int. Ed.*, 2021, **60**, 22265–22269, DOI: 10.1002/anie.202108801.

24 L. Li, H. Niu, J. Robertson, Z. Jiang, Y. Guo and C. Kuai, *Electrochim. Acta*, 2023, **439**, 141574, DOI: 10.1016/j.electacta.2022.141574.

25 Y. Liang, H. Shen, J. Li, H. Zhao, J. Xu, H. Huang, S. Xu, X. Liang, W. Zhou and J. Guo, *Chem. Eng. J.*, 2024, **497**, 154775, DOI: 10.1016/j.cej.2024.154775.

26 K. Li, M. Liang, H. Wang, X. Wang, Y. Huang, J. Coelho, S. Pinilla, Y. Zhang, F. Qi, V. Nicolosi and Y. Xu, *Adv. Funct. Mater.*, 2020, **30**, 2000842, DOI: 10.1002/adfm.202000842.

27 Q. Zhao, Q. Zhu, J. Miao, P. Zhang, P. Wan, L. He and B. Xu, *Small*, 2019, **15**, 1904293, DOI: 10.1002/smll.201904293.

28 Q. Tao, M. Dahlqvist, J. Lu, S. Kota, R. Meshkian, J. Halim, J. Palisaitis, L. Hultman, M. W. Barsoum, P. O. A. Persson and J. Rosen, *Nat. Commun.*, 2017, **8**, 14949, DOI: 10.1038/ncomms14949.

29 S. Shi, B. Qian, X. Wu, H. Sun, H. Wang, H. B. Zhang, Z. Z. Yu and T. P. Russell, *Angew. Chem., Int. Ed.*, 2019, **58**, 18171–18176, DOI: 10.1002/anie.201908402.

30 M. Q. Zhao, X. Xie, C. E. Ren, T. Makaryan, B. Anasori, G. Wang and Y. Gogotsi, *Adv. Mater.*, 2017, **29**, 1702410, DOI: 10.1002/adma.201702410.

31 Y. Yue, N. Liu, Y. Ma, S. Wang, W. Liu, C. Luo, H. Zhang, F. Cheng, J. Rao, X. Hu, J. Su and Y. Gao, *ACS Nano*, 2018, **12**, 4224–4232, DOI: 10.1021/acsnano.7b07528.

32 Z. Lin, J. Liu, W. Peng, Y. Zhu, Y. Zhao, K. Jiang, M. Peng and Y. Tan, *ACS Nano*, 2020, **14**, 2109–2117, DOI: 10.1021/acsnano.9b08832.

33 R. Liu and W. Li, *ACS Omega*, 2018, **3**, 2609–2617, DOI: 10.1021/acsomega.7b02001.

34 H. Chen, X. Chen, C. Rong, X. Ma, B. Zhang and F. Z. Xuan, *Small*, 2025, **21**, e06824, DOI: 10.1002/smll.202506824.

35 Y. Wen, T. E. Rufford, X. Chen, N. Li, M. Lyu, L. Dai and L. Wang, *Nano Energy*, 2017, **38**, 368–376, DOI: 10.1016/j.nanoen.2017.06.009.

36 A. A. Emerenciano, R. M. do Nascimento, A. P. C. Barbosa, K. Ran, W. A. Meulenberg and J. Gonzalez-Julian, *Membranes*, 2022, **12**, 1025, DOI: 10.3390/membranes12101025.

37 Y. Ma, Y. Hu, Y. Wang, J. Yu, S. Song and Z. Hu, *ACS Appl. Nano Mater.*, 2024, **7**, 23485–23493, DOI: 10.1021/acsanm.4c03315.

38 F. Ren, J. Zhang, T. Wu, F. Zhang, Z. Guo, Y. Jin and P. Ren, *Cellulose*, 2024, **31**, 2341–2353, DOI: 10.1007/s10570-024-05736-9.

39 D. Wang, Y. Peng, J. Dong, L. Pu, K. Chang, X.-P. Yan, H.-L. Qian, L. Li, Y. Huang and T. Liu, *Compos. Commun.*, 2023, **37**, 101429, DOI: 10.1016/j.coco.2022.101429.

40 X.-A. Ye, S.-Y. Zhang, D.-Q. Zhao, L. Ding, K. Fang, X. Zhou and G.-G. Wang, *Compos. A Appl. Sci. Manuf.*, 2024, **176**, 107866, DOI: 10.1016/j.compositesa.2023.107866.

41 W. Lee, M. Kim and J. Kim, *Compos. Sci. Technol.*, 2024, **257**, 110834, DOI: 10.1016/j.compscitech.2024.110834.

42 J. Huang, H. Wu and Z. Su, *J. Mater. Chem. A*, 2025, **13**, 23882–23892, DOI: 10.1039/d5ta01915j.

43 Z. Li, J. Li, B. Wu, H. Wei, H. Guo, Z. M. El-Bahy, B. Liu, M. He, S. Melhi, X. Shi, S. D. Mekkey, Y. Sun, B. B. Xu and Z. Guo, *J. Mater. Sci. Technol.*, 2024, **203**, 201–210, DOI: 10.1016/j.jmst.2024.02.084.

44 H. M. Cao, Y. D. Zhang, K. Zhang, J. Yu, L. Li, X. Chen and X. Z. Zhou, *Sci. China Mater.*, 2026, **69**, 308–318, DOI: 10.1007/s40843-025-3841-6.

45 Y. Luo, S. Jia, Y. Yi, X. Liu, G. Zhang, H. Yang, W. Li, J. Wang and X. Li, *J. Alloys Compd.*, 2024, **977**, 173355, DOI: 10.1016/j.jallcom.2023.173355.

46 T. Vlad-Bubulac, D. Serbezeanu, E. Perju, D. M. Suflet, D. Rusu, G. Lisa, T. A. Filip and M. A. Olariu, *Nanomaterials*, 2025, **15**, 1251, DOI: 10.3390/nano15161251.

47 J. Lin, C. W. Chang, C. T. Chang, K. Manibalan, T. H. Tsai, Y. C. Lin, Y. S. Hsu, M. H. Chang and J. T. Chen, *Chem. Commun.*, 2025, **61**, 10578–10581, DOI: 10.1039/d5cc01418b.

48 S. Yao, J. Jiang, Q. He, M. Chen, J. Luo, B. Zhong and Z. Jia, *Carbohydr. Polym.*, 2025, **368**, 124104, DOI: 10.1016/j.carbpol.2025.124104.

49 H. Hwang, S. Byun, S. Yuk, S. Kim, S. H. Song and D. Lee, *Appl. Surf. Sci.*, 2021, **556**, 149710, DOI: 10.1016/j.apsusc.2021.149710.

50 X. W. Ning, H. Huang, Y. F. Zhang, Z. H. Chen, Y. Guo, C. W. Li, Z. Fan, H. Tong and L. J. Pan, *Electrochim. Acta*, 2022, **435**, 141369, DOI: 10.1016/j.electacta.2022.141369.

51 Y. Wang, Z. L. Luo, Y. Q. Qian, W. Zhang and L. Z. Chen, *Chem. Eng. J.*, 2023, **454**, 140513, DOI: 10.1016/j.cej.2022.140513.

52 X. M. Wu, B. Huang, R. Y. Lv, Q. G. Wang and Y. Wang, *Chem. Eng. J.*, 2019, **378**, 122246, DOI: 10.1016/j.cej.2019.122246.

53 Z. B. Yang, Y. Wang, Y. R. Hu, Y. T. Zhuang, X. X. Ji, G. H. Yang and M. He, *Int. J. Biol. Macromol.*, 2023, **243**, 124828, DOI: 10.1016/j.ijbiomac.2023.124828.

54 M. Zhang, H. X. Yuan, B. Sun, Z. H. Lin, J. J. Chang and Y. Hao, *Nanotechnology*, 2025, **36**, 485402, DOI: 10.1088/1361-6528/ae1dff.

55 W. W. Zhao, J. L. Peng, W. K. Wang, B. B. Jin, T. T. Chen, S. J. Liu, Q. Zhao and W. Huang, *Small*, 2019, **15**, 1901351, DOI: 10.1002/smll.201901351.

56 W. J. Yu, Y. Li, B. J. Xin and Z. Lu, *Fibers Polym.*, 2022, **23**, 2994–3001, DOI: 10.1007/s12221-022-4389-4.

57 T. T. Duong, S. H. Kim and J. Kim, *J. Mater. Chem. A*, 2026, **14**, 4801–4812, DOI: 10.1039/d5ta06789h.

58 Z. B. Yang, Y. Lu, M. He, Y. Qi, G. H. Yang, J. C. Chen, Y. Wang and O. J. Rojas, *Cellulose*, 2025, **32**, 7131–7143, DOI: 10.1007/s10570-025-06663-z.

59 M. Depijan, K. Hantanasirisakul and P. Pakawatpanurut, *ACS Omega*, 2024, **9**, 22256–22264, DOI: 10.1021/acsomega.4c01353.

60 S. Ren, J. L. Xu, L. Cheng, X. Gao and S. D. Wang, *ACS Appl. Mater. Inter.*, 2021, **13**, 35878–35888, DOI: 10.1021/acsami.1c06161.

61 J. Acharya, G. P. Ojha, B.-S. Kim, B. Pant and M. Park, *ACS Appl. Mater. Inter.*, 2021, **13**, 17487–17500, DOI: 10.1021/acsami.1c00137.

62 H. Lindström, S. Södergren, A. Solbrand, H. Rensmo, J. Hjelm, A. Hagfeldt and S.-E. Lindquist, *J. Phys. Chem. B*, 1997, **101**, 7710–7716, DOI: 10.1021/jp970489r.

63 T. C. Liu, W. G. Pell, B. E. Conway and S. L. Roberson, *J. Electrochem. Soc.*, 1998, **145**, 1882–1888, DOI: 10.1149/1.1838571.